ADVANCED MATERIALS INTERFACES
Open Access
www.advmatinterfaces.de

Effect of Stack Pressure on the Microstructure and Ionic Conductivity of the Slurry-Processed Solid Electrolyte Li_7SiPS_8

*Duc Hien Nguyen, Markus Osenberg, Christian Schneider, Julian Moosmann, Felix Beckmann, Ingo Manke, and Bettina V. Lotsch**

All-solid-state batteries (ASSBs) have gained much interest in recent years because they promise higher energy and power densities as well as improved safety over lithium-ion batteries (LIBs). This is achieved by using non-flammable solid electrolytes (SEs) together with lithium metal or high-capacity silicon anodes. One major hurdle to overcome is the permanent intimate contact of all cell components to enable long-term cycling stability. This study investigates the macroscopic (microstructure) and microscopic (atomistic) effects of uniaxial stack pressure on the transport properties of free-standing, slurry-processed tetragonal Li_7SiPS_8 (*t*-Li_7SiPS_8) sheets, containing different solid electrolyte (SE)-to-binder ratios (SE:B) and particle size fractions. The results demonstrate that binder content and particle size significantly influence the morphology as evidenced by synchrotron-radiation computed tomography (CT), pressure response, and ionic conductivity of the sheets. Notably, while compression mechanics are consistent across samples, relative densities, and ionic conductivities are more dependent on binder content than particle size. Larger particles and lower binder contents generally led to higher ionic conductivities. The study also reveals that activation volumes appear to increase with binder content, suggesting that extrinsic factors, particularly the binder, may obscure the calculation of the intrinsic activation volumes of *t*-Li_7SiPS_8. Thus, the obtained values for binder-containing sheets may be considered apparent values. Contrary to expectations, repeated compression cycles led to a decreased ionic conductivity and relative density, likely due to microstructural damage and increased (apparent) activation volumes. Overall, the study serves as a reminder to the community to carefully interpret intrinsic values, such as the activation volume, and by extension the activation energy, in the increasingly popular binder-containing SE sheet systems.

1. Introduction

As of today, lithium-ion batteries (LIBs) are the leading technology for electrical energy storage and are widely used in most electronic devices due to their high reliability and long cycle life.[1–3] With increasing demands for higher energy densities and safety, however, the need for alternative energy storage technologies beyond LIBs is steadily growing. One promising candidate is the all-solid-state battery (ASSB), in which the conventional organic solvent-based electrolyte is replaced by a solid electrolyte (SE). The ASSB-technology promises not only a higher safety owing to the non-flammability of the SE but also higher energy densities above 500 Wh kg^{-1} and fast charging,[4–6] if Li-metal anodes[7–9] and high capacity cathode materials (e.g. transition metal oxides[10–12] or sulfur[13,14]) are used. Contrary to liquid electrolytes, which ensure good interfacial contact between particles and electrodes, SEs often face challenges in maintaining optimal interfacial contact due to their rigid nature, especially during operation, where volume changes can occur. By applying external pressure, the solid components can be deformed and their interfaces modified so that contact loss between

D. H. Nguyen, C. Schneider, B. V. Lotsch
Max Planck Institute for Solid State Research
Heisenbergstraße 1, 70569 Stuttgart, Germany
E-mail: b.lotsch@fkf.mpg.de

The ORCID identification number(s) for the author(s) of this article can be found under https://doi.org/10.1002/admi.202500845

DOI: 10.1002/admi.202500845

D. H. Nguyen, B. V. Lotsch
LMU Munich
Butenandstraße 5-13, 81377 Munich, Germany
M. Osenberg, I. Manke
Helmholtz-Zentrum Berlin für Materialien und Energie (HZB)
Hahn-Meitner-Platz 1, 14109 Berlin, Germany
J. Moosmann, F. Beckmann
Helmholtz-Zentrum Hereon
Max-Planck-Str. 1, 21502 Geesthacht, Germany
B. V. Lotsch
Cluster of Excellence e-conversion
Lichtenbergstraße 4a, 85748 Garching, Germany

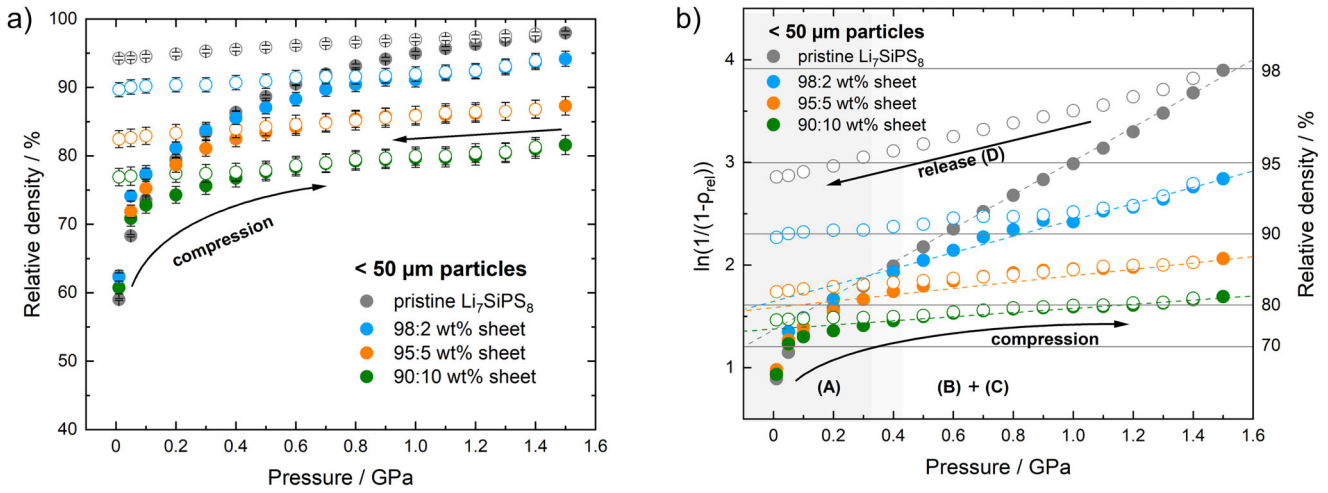

Figure 1. a) Evolution of relative densities of pristine *t*-Li_7SiPS_8 and *t*-Li_7SiPS_8-based sheets containing different binder weight fractions with varying pressure. The samples consist of < 50 µm particles. b) Heckel plot analysis of the same samples shown in (a). The gray shaded area up to 0.4 GPa corresponds to particle rearrangement (A), whereas the white area corresponds to plastic deformation (B) and likely minor elastic deformation (C) during compression. The dashed lines indicate the linear regime in phase (B), while the horizontal lines serve as an aid to estimate the relative densities of the samples. Filled and hollow data points correspond to the compression cycle and the pressure release (decompression) cycle, respectively.

particles and microstructural cracking is minimized. This step is critical for achieving excellent cyclability, as it enables intimate contact, promoting efficient electronic and ionic transport.[15]

A distinction is made between two types of external pressure, namely fabrication and stack pressure. Fabrication pressure describes the pressure typically applied during the manufacturing process of electrodes and SE-based separators. It involves the improvement of density and internal contacts within the powdered starting materials and includes isostatic or uniaxial (cold) pressing of the SE and electrode pellets and/or calendering (roll pressing). Stack pressure denotes the constant pressure applied during measurement/operation and is responsible for keeping cell components together, reducing the dead space between single cells, and enhancing the contact between electrodes and SEs. In recent years, the effect of (stack) pressure on SEs, especially on thiophosphates (e.g., $Li_{10}GeP_2S_{12}$ (LGPS))[16,17] and lithium argyrodites (e.g., Li_6PS_5Cl (LPSCl)),[18,19] has gained more attention, owing to their mechanically soft properties.[20–22] These studies showcase the need for detailed reporting of experimental parameters, like pressure, to better compare and evaluate key performance indicators of SE.[23] Especially the ionic conductivity of SEs can vary between orders of magnitude within a material, as shown by previous works.[24,25] Indeed, significant insights on the influence of pressure have been gained on, for example, the initial discharge capacity with improved capacity retention[26–30] due to the enhanced contact of the electrodes and SEs during cycling.[31–35] Other studies showed reduced Li dendrite formation[36–39] and enhanced cyclability with Li-metal ASSBs[19,40,41], to name just a few. In a recent systematic study on LGPS-like fast ion-conducting tetragonal Li_7SiPS_8 (*t*-Li_7SiPS_8) we disentangled macroscopic from microscopic effects on the ionic conductivity, supported by simulations based on the discrete element method (DEM) and finite volume analysis (FVA).[42] Taking this study as a blueprint, we systematically investigate the macroscopic (microstructure) and microscopic (atomistic) effects of the stack pressure on the density and impedance of slurry-processed *t*-Li_7SiPS_8 sheets with varying binder contents and particle size fractions. Our findings indicate that both binder content and particle size significantly affect the sheets' morphology and pressure behavior as confirmed by synchrotron tomography, with all samples following the empirical Heckel equation for powder compression, revealing distinct compaction regimes. Additionally, electrochemical impedance spectroscopy (EIS) measurements – conducted under single and repeated compression/decompression cycles – demonstrate that the ionic conductivity shows a maximum in a certain stack pressure range, and is strongly influenced by binder content and particle size, while extrinsic factors, i.e., binder, likely influence the derived (apparent) activation volumes.

2. Results and Discussion

2.1. Effect of Binder Content and Particle Size on the Compression Behavior of *t*-Li_7SiPS_8 Sheets

Figure 1a compares the evolution of relative densities with applied variable pressure on sheets with different binder contents, as well as on a pristine powder sample (exemplary for < 50 µm particles). The relative densities of the samples consisting of larger particle size fractions are summarized in Figure S3 (Supporting Information). To understand the underlying compaction mechanism of the *t*-Li_7SiPS_8 sheets, we first need to mention the Heckel equation[43] derived from the compaction of metal powders, which is as follows:

$$\ln\left(\frac{1}{1-\rho_{\mathrm{rel}}}\right) = Kp + A, \tag{1}$$

where ρ_{rel} is the relative density of the sample at pressure *p*. *K* and *A* are the slope and y-intercept of the linear region of the Heckel plot (Figure 1b), respectively.

For a more in-depth description of the Heckel plot, we refer to the Supporting Information and the study by Schneider et al.[42]

The samples show a sharp increase in relative density, which is accompanied by an initial curvature due to particle rearrangement (phase A) up to approximately 0.4 GPa. Above 0.4 GPa, we observe a linear increase (dashed lines), which is reminiscent of plastic deformation (phase B). By calculating the inverse of the slope K of the dashed lines, the resulting value serves as the mean yield pressure P_m of the material, which describes the stress required for the material to deform plastically.[43–46] The P_m of 0.59(3) GPa for the pristine sample increases to 1.31(5) GPa for the 98:2 wt%, to 3.92(4) GPa for the 95:5 wt%, and to 5.62(4) GPa for 90:10 wt% sheets. These results indicate easier plastic deformation for pristine samples and, inversely, more difficult plastic deformation for sheets with increasing binder content. The final elastic deformation phase (C) at high pressure is often characterized by an upward curvature,[47,48] which is not observed in our samples. It is possible that either not high enough pressures were applied for this phase to occur or, more likely, that elastic deformation takes place during phase (B). Lastly, in the final phase of decreasing the pressure – the elastic recovery phase (D) – the sample relaxes into its final dimensions.[49,50]

With the knowledge of how to interpret the different phases in the Heckel plot in mind, we can take a look at Figure 1 in more detail. We notice that all samples show an initial relative density of about 60% and a sharp non-linear increase, typical for particle rearrangement, in phase (A) until about 0.4 GPa. A larger increase in relative density is observed for the pristine sample (or low binder content sheets) compared to the high binder content sheet. Two possible explanations exist: first, a statistically greater number of rearrangements of loose particles occurs, as more individual particles are present in the same sample mass per volume in the pristine case, compared to the sheets. Second, the binder fixates individual SE particles, impeding rearrangement. These two effects are more pronounced the more binder is present in the sample. The highest relative density is observed for pristine *t*-Li_7SiPS_8, reaching up to 98%, followed by the 98:2 wt% sheet with roughly 94%. The higher binder-containing sheets reach their maximum relative densities at around 87% for 95:5 wt% sheets and at around 83% for 90:10 wt% sheets. When the pressure is released, the final relative densities are on average 3-4 % lower than the corresponding maximum relative densities. We conclude that the presence of the binder prevents the sheet from reaching as high relative densities as compared to the pristine sample and that the amount of binder determines the final relative density.

2.2. Influence of In-Situ Uniaxial Pressure on the Ionic Conductivity of *t*-Li_7SiPS_8 Sheets

To investigate the effect of the uniaxially applied pressure on the ionic conductivities of the samples, electrochemical impedance spectroscopy (EIS) measurements were conducted at different stack pressures at room temperature and are summarized in **Figure 2**.

The highest ionic conductivities (approximately 7 mS cm^{-1}) are observed for pristine *t*-Li_7SiPS_8 between 0.1 – 0.2 GPa. Unlike the sheets, which were slurry-processed and thus came in contact with solvent, the pristine samples were not treated with solvent, which is known to negatively affect the ionic conductivity. Therefore, it is expected that pristine samples should exhibit higher conductivities.[51] Furthermore, the binder content influences the maximum attainable ionic conductivity, with low binder content sheets showing higher conductivities.[52,53] The 98:2 wt% sheets reach peak conductivities up to 4 mS cm^{-1} between 0.2–0.5 GPa. In comparison, the 90:10 wt% sheets exhibit conductivities up to 1 mS cm^{-1} in the same pressure range, while the conductivity values of the 95:5 wt% sheets lie between those of 90:10 wt% and 98:2 wt% sheets.

Generally, lower conductivities are measured for sheets consisting of smaller-sized particles (Figure 2c), as compared to the sheets containing 50 – 100 µm (Figure 2b) or > 100 µm (Figure 2c) particle sizes. This observation is consistent with a previous study, where also higher Li diffusivities were found in such sheets and can be explained by fewer inter-particle grain boundaries and binder contributions that both negatively affect ion transport.[54]

Independent of the binder content and particle size, the highest ionic conductivities are usually observed between 0.2-0.5 GPa for the sheets and 0.1-0.2 GPa for the pristine samples. Beyond these pressure values, we notice a decrease in conductivity due to the molar volume compression of the unit cell, which will be explained in the following section. When the pressure is released (decompression), we observe that the conductivities at high stack pressures tend to be lower than during the compression cycle. We attribute this to the so-called "springback" effect stemming from the internal relaxation of the SE particles and binder after pressure release causing microstructural contact loss between the SE particles, as observed in previous studies.[52,55] However, it is observed that the conductivities obtained during decompression at low stack pressures are significantly higher than during compression, especially for the pristine samples.

The final conductivities obtained at the last release step (0.01 GPa) differ a lot depending on the binder content. Low binder sheets (98:2 wt%) prove to be better than high binder sheets (90:10 wt%) in terms of conductivity. The values are between 1.5 – 2 mS cm^{-1}, which are on average four to five times higher than those of the 90:10 wt% sheets (approximately 0.4 mS cm^{-1}).

Exemplary Nyquist plots of 90:10 wt% sheets (< 50 µm particles) obtained at various stack pressures in the release cycle (decompression) are shown in Figure 2d. Here, we observe decreasing resistances with decreasing pressure from 1.5 until 0.4 GPa. This is attributed to the relaxation of the unit cell after compression for better Li diffusion. From 0.3 GPa the resistance increases again, likely due to less benign (i.e., less conformal) contacts within the sample and to the electrode.

2.3. Influence of Uniaxially Applied Pressure on the Activation Volume of *t*-Li_7SiPS_8 Sheets

As described above, the ionic conductivity first increases non-linearly with increasing pressure - the reason for this being particle rearrangement and fragmentation - until it reaches a maximum. The peak conductivities are generally observed between 0.2 – 0.5 GPa, independent of the binder content and particle

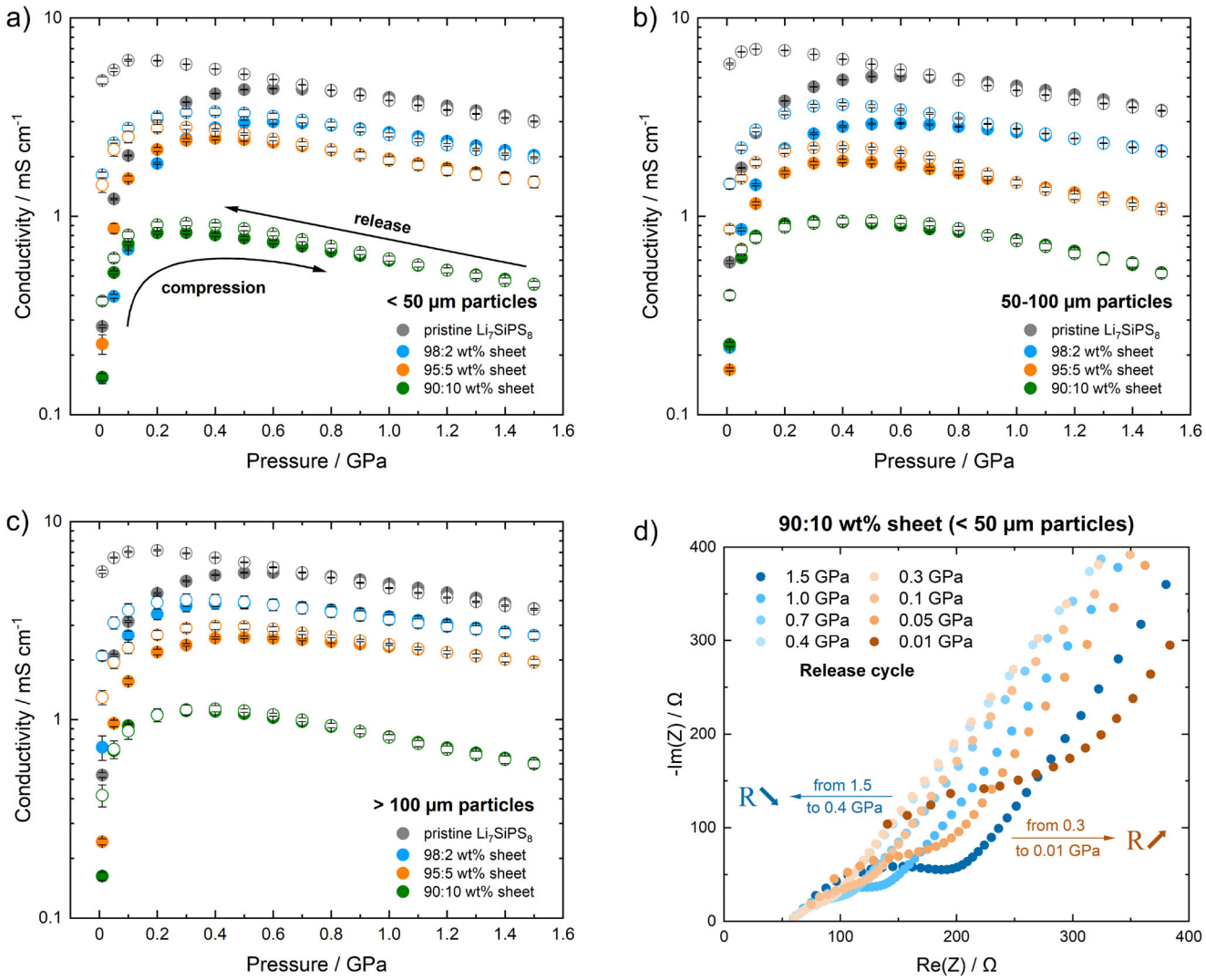

Figure 2. Evolution of the total ionic conductivities of pristine *t*-Li_7SiPS_8 and *t*-Li_7SiPS_8-based sheets containing different binder weight fractions and different particle sizes of a) < 50 µm, b) 50 – 100 µm, and c) > 100 µm with varying stack pressure. Filled and hollow data points correspond to the compression cycle and the release (decompression) cycle, respectively. d) Exemplary Nyquist plots of a *t*-Li_7SiPS_8-based sheet with 10 wt% binder content and composed of < 50 µm particles during the pressure release cycle. Decreasing impedance is indicated by the different blue-shaded data points from 1.5 to 0.4 GPa, while increasing impedance is indicated by the different orange-shaded data points from 0.3 to 0.01 GPa.

size. Above this pressure range, a decrease in ionic conductivity is observed. Here, elastic molar volume compression takes place. The resulting compressed unit cell of *t*-Li_7SiPS_8 shows lower Li diffusion, which was previously confirmed via ab initio molecular dynamics (AIMD) simulations and discussed in detail by Schneider et al.[42] In essence, the dependence of the ionic conductivity on (stack) pressure is linked to the activation volume ΔV, which can be calculated using

$$\Delta V \approx -k_B T \left(\frac{\partial \ln(\sigma)}{\partial p} \right)_{T,N_i} \quad (2)$$

where k_b is the Boltzmann constant and T is the temperature. The activation volume describes the difference between the volume that is required by a mobile species (here Li-ion) to migrate from one site to another (V_m) and the free volume provided by the (anionic) sublattice (V_f):

$$\Delta V = V_m - V_f \quad (3)$$

Any non-zero activation volume indicates an imbalance between the free volume of the structure and the required migration volume. Positive activation volumes are obtained when the lattice has to locally expand for the migrating ion to pass through, which would otherwise be too narrow for its size.[56–59] The activation volume usually becomes negative when ion transport improves with increasing pressure.[60,61]

When the pressure is plotted against $\ln(\sigma)$, we can estimate the activation volume from the fitted slope as shown exemplarily in **Figure 3a** for the < 50 µm particles containing samples.

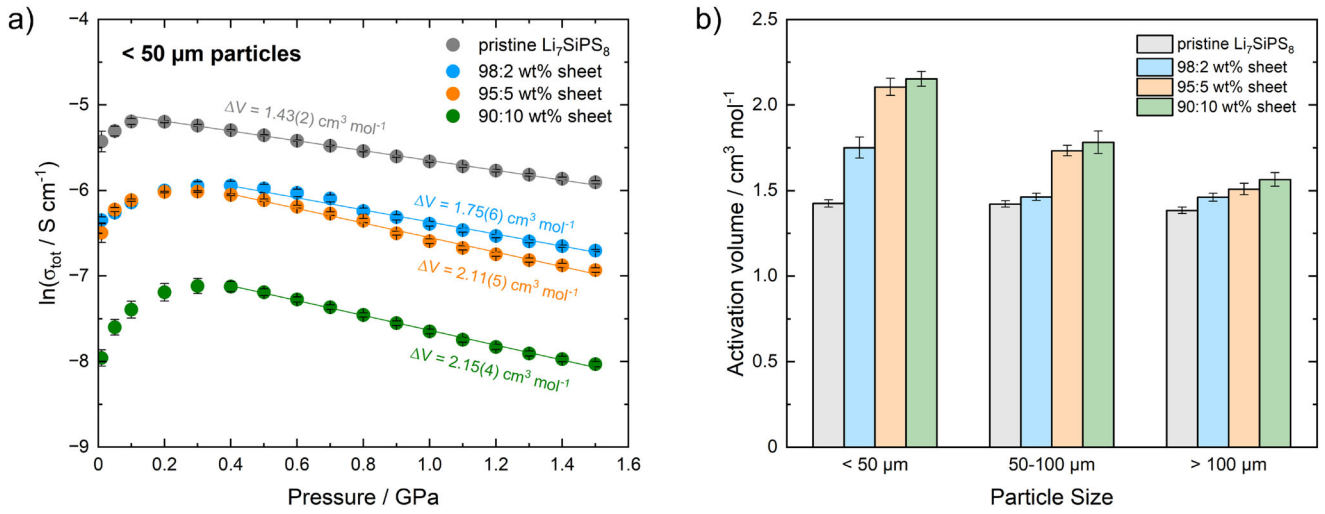

Figure 3. a) Natural logarithm of the total ionic conductivities obtained in the pressure release cycles of pristine *t*-Li_7SiPS_8 and *t*-Li_7SiPS_8-basedsheets containing different binder weight fractions. The samples consist of < 50 µm particles. From the fitted slopes the activation volumes of *t*-Li_7SiPS_8 in each sample can be calculated. b) Comparison of the activation volumes of pristine *t*-Li_7SiPS_8 and *t*-Li_7SiPS_8-based sheets containing different binder weight fractions with different particle size fractions.

This results in an activation volume of approximately 1.42(2) cm^3mol^{-1} for the pristine sample, which is in agreement with the literature.[42] While for the 98:2 wt% sheet an activation volume of 1.75(6) cm^3mol^{-1} is estimated, the value increases to 2.11(5) cm^3mol^{-1} for the 95:5 wt% sheet and to 2.15(4) cm^3mol^{-1} for the 90:10 wt% sheet. Figure 3b categorizes the activation volumes of *t*-Li_7SiPS_8 in all samples relative to the different particle size fractions.

We observe similar activation volumes for the pristine *t*-Li_7SiPS_8 samples irrespective of their particle sizes (gray bars). From this, we can exclude any significant correlation between the activation volume and the particle size fraction. Considering that the activation volume is fundamentally an intrinsic material property, it should not depend on extrinsic factors like size or form. However, this changes for the sheets, where we, first, observe higher activation volumes compared to the pristine samples and, second, increasing activation volumes with increasing binder content. When comparing only the sheets, the highest activation volumes are generally calculated for sheets composed of <50 µm particles, whereas the corresponding sheets incorporating >100 µm particles tend to show lower values. For example, for the 90:10 wt% sheet consisting of >100 µm particles, an activation volume of 1.56(4) cm^3mol^{-1} is estimated, which is just 10% higher than the value of the pristine sample. In contrast, the same sheet composition with <50 µm particles has an approximately 50% higher value with 2.15(4) cm^3mol^{-1}. The activation volumes of *t*-Li_7SiPS_8 in the sheets containing 50 − 100 µm particles fall between those of <50 µm and >100 µm particle-sized sheets.

It seems that the activation volume of *t*-Li_7SiPS_8 calculated from the sheets is affected by both the particle size fraction and the binder content. However, given the insensitivity of the activation volume to the particle size in the pristine sample, the observed effects may be related to the particle size only indirectly and be predominantly related to the presence of the binder. It is thus reasonable to attribute the observations to external factors such as the samples' microstructure, and particularly the ratio of surface area to volume exposed to the binder. Despite the same amount of binder, the surface area of <50 µm particles with respect to their volume is much larger than that of >100 µm particles, hence, interacting more extensively with the binder. Conversely, the ratio of surface area to volume of >100 µm particles is much smaller than that of <50 µm particles, resulting in fewer particles being affected by the binder. We need to emphasize that the activation volume is a material-specific, i.e., intrinsic property, which should not be influenced by the (non-conducting) binder. The fact that we do observe a deviation from the reference value of the pristine sample thus leads to the assumption that the sheets' activation volumes have to be considered as apparent, rather than intrinsic values upon binder incorporation. We use the term "apparent" activation volume here, since we assume that the presence of the binder makes it more difficult to access the "true" intrinsic values of *t*-Li_7SiPS_8 in such sheets. Even though the binder plays a significant role, its contribution to the calculation of the activation volume is not directly captured by equation (2). The activation volume is derived from the ionic conductivity, which itself is influenced by a myriad of factors, including the microstructure.

2.4. Particle-Size Evolution Observed by 3D Synchrotron CT

To complement the electrochemical and mechanical analyses, we investigated the particle-size distribution (PSD) and microstructural evolution of the *t*-Li_7SiPS_8 sheets using synchrotron-radiation-based X-ray computed tomography (CT). For the sheet compositions containing high/low binder amounts and large/small particles, representative 3D volume reconstructions were acquired both before and after applying the target uniaxial stack pressure (1.5 GPa). Through segmentation of the CT data, we successfully distinguished the solid *t*-Li_7SiPS_8 phase, binder-rich regions, and pore spaces as shown in **Figure 4**.

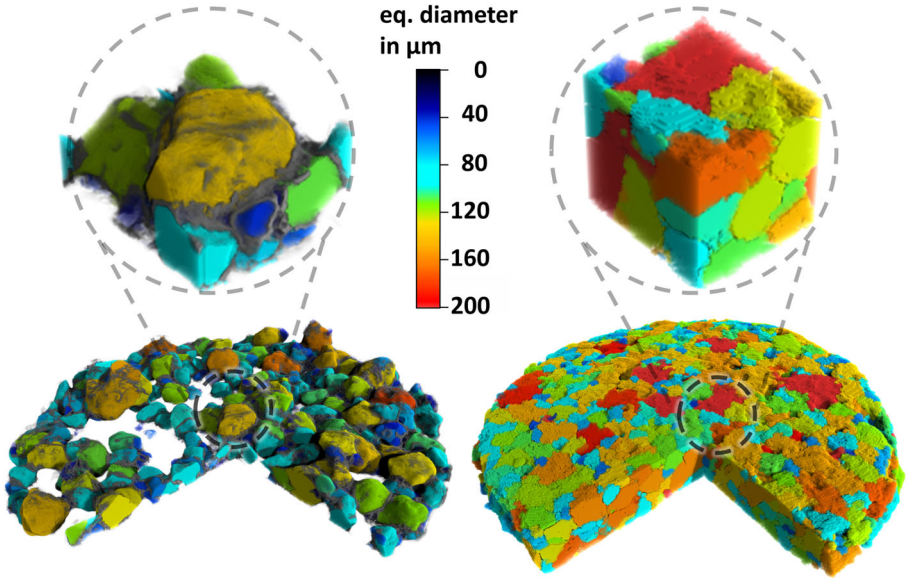

Figure 4. Two example 3D renderings of 90:10 wt% sheets (>100 µm particles) before (left) and after (right) compression. The particles are colored according to their diameter. In the uncompressed state the binder could be segmented and is shown in gray.

The PSDs of the *t*-Li_7SiPS_8 particles were then quantified by calculating the equivalent spherical diameter of each segmented particle within the 3D volumes. These volume-weighted PSDs were subsequently Gaussian-fitted to extract key parameters: the mean equivalent diameter (x_c) and the distribution width (w) of secondary particles before and after compression. A summary of these parameters for the different compositions, along with the corresponding fitted distributions, is presented in **Figure 5**.

As expected, the initial PSDs reflected the nominal particle-size fractions: the small-particle sheets exhibited mean diameters of approximately 23.57 ± 0.07 µm (high binder) and 22.75 ± 0.09 µm (low binder), while the large-particle sheets showed significantly larger mean diameters of about 100.6 ± 2.0 µm (high binder) and 72.3 ± 1.5 µm (low binder). The distribution widths (w) ranged from roughly 13.7 – 13.9µm for small-particle samples to 66.2 – 70.4µm for large-particle samples before compression.

After uniaxial compression, the PSD evolution was strongly dependent on both binder content and initial particle size. In the high-binder samples, the mean diameter x_c decreased significantly, from 23.57 µm to 19.94 µm for the small-particle sheet (a reduction of 3.63 µm or 15.4%) and from 100.6 to 76.0 µm for the large-particle sheet (a reduction of 24.6 µm or 24.5%). Correspondingly, the distribution width w narrowed from 70.4 µm to 35.6 µm (a 49.4% decrease) in the large-particle, high-binder sample, indicating fragmentation into a more uniform, but overall smaller particle population. The small-particle, high-binder sample showed a minor decrease in w from 13.93 µm to 13.44 µm (about 3.5%).

Conversely, in the low-binder sheets, PSD changes varied with particle size. The large-particle, low-binder sheet exhibited negligible change in mean diameter (x_c)—from 72.3 µm to 73.0 µm, a 1.0% increase within measurement uncertainty—while the distribution width decreased markedly from 66.2 µm to 47.4 µm (a 28.4% reduction), suggesting elimination of extreme

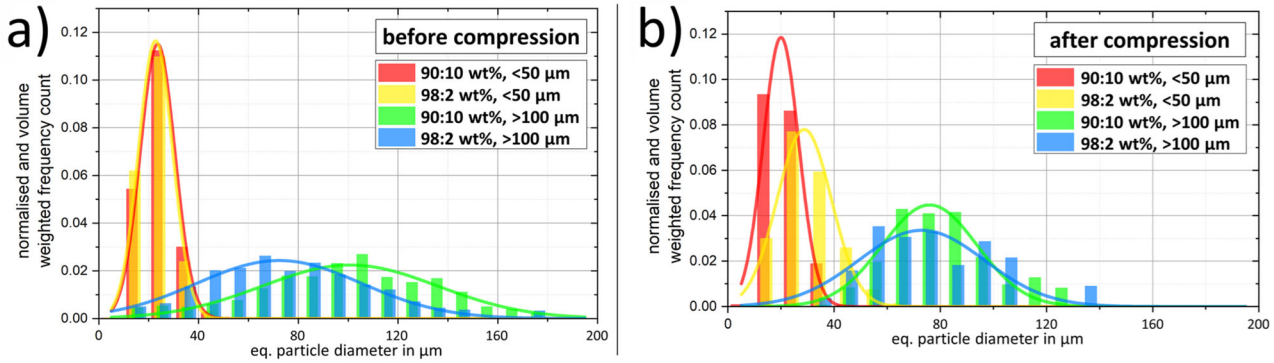

Figure 5. Volume weighted particle-size distributions representing the before and after compression state of *t*-Li_7SiPS_8 sheets with differing particle sizes (>100 µm vs. < 50 µm) and binder contents (98:2 wt% vs. 90:10 wt%). a) Shows "before" state and b) the "after-compression" state. The parameters of the respective Gaussian fits are listed in the Supporting Information in Table S2.

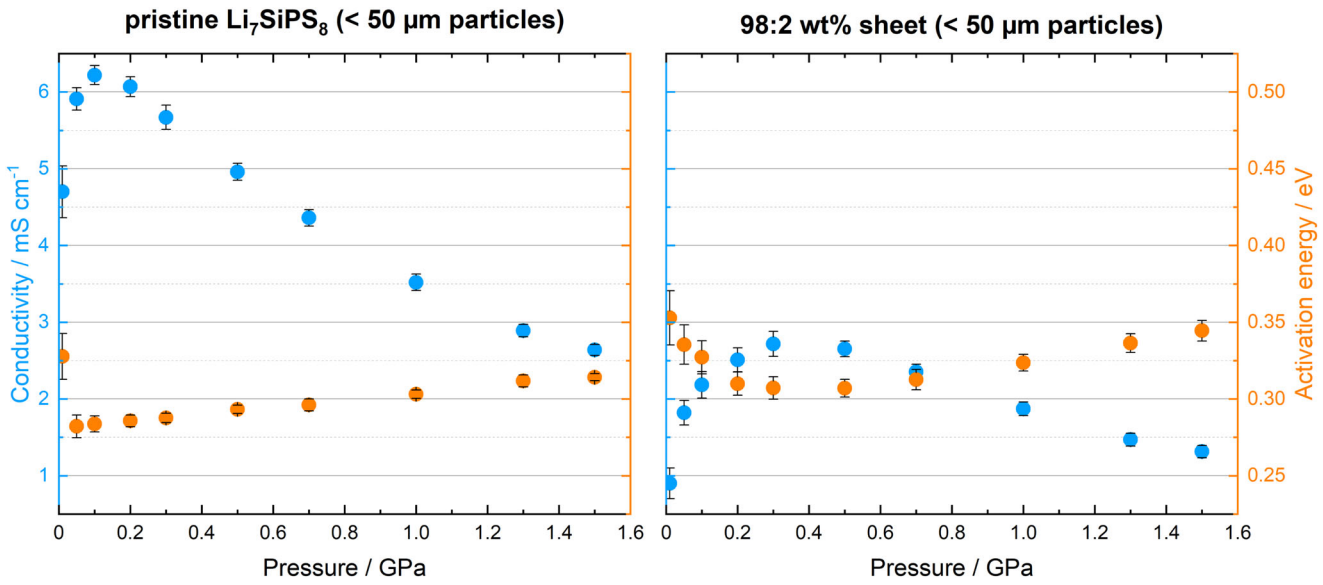

Figure 6. Evolution of the total ionic conductivities (blue) and activation energies (orange) of pristine *t*-Li_7SiPS_8 (left graph) and *t*-Li_7SiPS_8-based sheet with 98:2 wt% (right graph) with varying pressure at 20 °C. Both samples consist of <50 µm particles.

particle sizes but retention of the bulk particle size. In stark contrast, the small-particle, low-binder sheet experienced a significant increase in x_c from 22.75 µm to 28.70 µm, corresponding to a 26.1% increase, accompanied by a substantial broadening of the PSD width from 13.71 to 20.46 µm (a 49.2% increase). This indicates that particle rearrangement and agglomeration likely dominated over fragmentation in this sample.

These trends suggest that high binder content consistently promotes fragmentation under compression, reducing mean particle size and narrowing distributions, particularly evident in both particle size fractions. Meanwhile, low binder content permits different behaviors depending on initial particle size: large-particle sheets maintain their mean size with some narrowing of the size distribution, whereas small-particle sheets show an effective growth of particle size and PSD broadening, likely due to agglomeration or binder bridging effects.

Overall, these microstructural evolutions directly impact the density and connectivity of particle interfaces and grain boundaries, which are critical factors influencing ionic conduction pathways and thus transport properties. The fragmentation observed in high-binder sheets is consistent with increased grain boundary resistance and higher apparent activation volumes, while the agglomeration tendencies in low-binder, small-particle sheets could improve particle contact and enhance percolation pathways or affect tortuosity in complex ways, as further discussed in the subsequent section.

2.5. Temperature-Dependent EIS Measurements at Different Pressures

In addition to the pressure-dependent EIS studies at room temperature, temperature-dependent EIS studies at variable stack pressures were conducted. The total ionic conductivity σ_{tot} shows a temperature dependence, thus, the activation energy E_A can be derived from the Arrhenius-type equation:

$$\sigma_{tot} T = \sigma_0 \exp\left(-\frac{E_A}{k_B T}\right) \quad (4)$$

where σ_0 is the pre-exponential factor, k_B is the Boltzmann constant, and lastly T is the temperature. Exemplary Arrhenius plots of the 98:2 wt% sheet (<50 µm particles) at different pressure values are depicted in Figure S10 (Supporting Information). From the slope, the activation energy at each pressure can be extracted, while the pre-exponential factor can be obtained from the y-intercept.

Figure 6 summarizes the evolution of the activation energy and conductivity with pressure at 20 °C of pristine *t*-Li_7SiPS_8 (left side) and the 98:2 wt% sheet (right side). Taking a closer look at the data of the pristine sample, at the initial pressure of 0.01 GPa, an activation energy of 0.33 eV and an ionic conductivity of approximately 4.7 mS cm^{-1} is obtained. The larger error bar associated with these values is attributed to the poor contacts within the sample and with the electrode at low pressure. With increasing pressure, a decrease in activation energy is observed, reaching a minimum of 0.28 eV between 0.05-0.1 GPa. Contrary, the ionic conductivity reaches its peak of 6.1 mS cm^{-1} at 0.1 GPa. As the pressure increases, the effect of elastic deformation results in a decrease in conductivity to 2.4 mS cm^{-1}, while the activation energy increases to 0.31 eV at 1.5 GPa. Similar trends are observed for the 98:2 wt% sheet albeit with lower conductivities and higher activation energies. The conductivity increases from 0.9 mS cm^{-1} (at 0.01 GPa) to a peak conductivity of 2.7 mS cm^{-1} between 0.3–0.5 GPa, before a decrease to 1.3 mS cm^{-1} at 1.5 GPa is observed. It is noteworthy that the sheets' activation energies are consistently about 20 – 30 meV higher than that of the pristine sample. As previously seen, the evolution of the activation energy with pressure inversely mirrors the behavior of the

conductivity. An increase in conductivity is accompanied by a decrease in activation energy, and vice versa.

Comparable findings are made with the samples consisting of >100 µm particles (Figure S11a, Supporting Information). The pristine sample (left side) displays a comparable behavior of both the conductivity and activation energy curves, with similar values to those observed in the <50 µm particle variant. Additionally, a more pronounced activation energy minimum of 0.26 eV at 0.05 GPa can be noticed. This minimum does not align with the peak conductivity (6.2 mS cm^{-1}), unlike with the <50 µm particles. Instead, the peak conductivity is found at a slightly higher pressure of 0.2 GPa.

The 98:2 wt% sheet composed of >100 µm particles (right side) shows a similar behavior with respect to the sheet made of <50 µm particles, and the activation energy values are comparable. The only difference is that the pressure range at which the activation energy minima and peak conductivities are found, shifts to higher values between 0.5–0.7 GPa. It appears that samples incorporating >100 µm particles require higher (stack) pressures before reaching peak conductivities. One possible reason may be the overall lower relative densities with such samples, as seen in Figure S3 (Supporting Information).

The 10 wt% binder-containing sheets were also explored and are summarized in Figure S11b (Supporting Information, < 50 µm left side, >100 µm right side). Overall, the conductivities show a similar behavior, albeit with even lower values than seen with the lower binder containing sheets. However, unlike before, the activation energies do not inversely scale with the conductivities and do not follow a clear trend. Instead, the values of the activation energy are higher, especially for the sheet with <50 µm particles, averaging at approximately 0.38 eV, albeit with significantly larger error bars. Interestingly, a parallel increase of conductivity and activation energy until approximately 0.4 GPa can be noticed. The activation energies for the sheet composed of > 100 µm (right side) are slightly lower, with 0.34 eV on average. It appears that for samples incorporating higher amounts of binder, the interpretation of the apparent activation volume and the activation energy is not straightforward.

Nonetheless, the evolution of conductivity and activation energy of the pristine and low binder-containing samples (excluding the high binder-containing sheets) hints at a strong correlation. Indeed, it is frequently observed that higher (ionic) conductivities are associated with lower activation energies, and vice versa. This was shown in previous studies, for example, where anion or cation substitution led to higher conductivities and lower activation energies for ion diffusion due to disorder in the anion lattice[62–64] or lattice softening through incorporation of larger, more polarizable anions.[65,66] In this context the Meyer–Neldel rule is relevant, which suggests that decreasing activation energies are often accompanied by lower pre-exponential factors, thereby compensating each other's influence on the ionic conductivity. This empirical observation is thus known as the "compensation rule" and is usually observed within a material class.[67] By plotting the activation energies against the pre-exponential factors, we observe a positive correlation, which is in agreement with the Meyer–Neldel rule (Figure S15, Supporting Information). Our study suggests that this correlation between E_A and σ_0 can also be seen by varying the pressure, in addition to the more commonly invoked elemental substitution as shown in previous studies.[62,68]

3. Conclusion

In this study, the macroscopic (i.e., microstructure) and microscopic (i.e., atomistic) effects of uniaxially applied stack pressure on the transport properties of free-standing *t*-Li_7SiPS_8 sheets composed of different SE:B ratios (98:2, 95:5, and 90:10 wt%) and particle size fractions (> 100 µm, 50 – 100 µm and <50 µm particles) were investigated.

Our findings revealed a significant influence of the binder content and particle size fraction on the morphology, pressure behavior, and ionic conductivity of the sheets. The sheets showed similar compression mechanics with distinct compression phases according to the empirical Heckel equation. The measured relative densities differ greatly, depending more on the binder content than on the particle size fraction. Furthermore, low binder containing sheets generally exhibited higher relative densities compared to high binder containing sheets, which is similarly reflected in the ionic conductivity. To achieve high ionic conductivities, the binder content should be kept as low as possible. The usage of larger particles is also beneficial for maximizing the ionic conductivity due to the lower number of inter-particle contacts, effectively reducing grain boundary resistances.

For all sheet samples, the peak ionic conductivities were generally observed between 0.2–0.5 GPa, with 98:2 wt% sheets showing an up to tenfold increase, reaching around 1.5 – 2 mS cm^{-1}. Beyond these pressure values, a decrease in ionic conductivity was observed across all sheet samples, which was attributed to the increasing atomistic effects of molar volume compression at high pressures.

Furthermore, we noticed a trend of increasing (apparent) activation volumes with increasing binder content. According to 3D synchrotron CT, high binder sheets experienced significant particle fragmentation, reducing the mean particle size and thus increasing grain boundary resistances. In contrast, low binder sheets either maintain their mean particle size (for >100 µm particles) or show a growth of particle size (for <50 µm particles) likely due to agglomeration or binder bridging effects.

In conclusion, we improved the slurry-processed *t*-Li_7SiPS_8 sheet in terms of composition and identified the optimal pressure range to maximize their ionic conductivity. Furthermore, our study revealed that parameters, such as the activation volume (and by extension the activation energy), may only be well interpreted in "pristine" cases, whereas in sheet systems, their interpretation is obscure and their values are likely to be of apparent nature. Thus, our study highlights the need to carefully interpret the performance metrics of the increasingly popular SE sheet systems.

Supporting Information

Supporting Information is available from the Wiley Online Library or from the author.

Acknowledgements

The authors acknowledge financial support by the Max Planck Society, the German Federal Ministry of Research and Education (BMBF), projects

03XP0177B (MPI-FestBatt I), 03XP0430B (MPI-FestBatt II), the Center for Nanoscience (CeNS) and the Deutsche Forschungsgemeinschaft via the Cluster of Excellence e-conversion (EXC2089). The authors gratitude go to Viola Duppel for SEM-EDX imaging. The authors acknowledge Deutsches Elektronen-Synchrotron DESY (Hamburg, Germany), a member of the Helmholtz Association HGF, for the provision of experimental facilities. Parts of this research were carried out at PETRA III. Data was collected using high-energy material science (HEMS) beamline P07 operated by Helmholtz-Zentrum Hereon related to beamtime proposal BAG-11020190. This research was supported in part through the Maxwell computational resources operated at DESY. We would like to thank Tobias Arlt and André Hilger for assistance during the DESY experiments and later data reconstructions. Beamtime was allocated for proposal 11020405.

Open access funding enabled and organized by Projekt DEAL.

Conflict of Interest

The authors declare no conflict of interest.

Author Contributions

D.H.N. contributed to the writing of the original draft, formal analysis, conceptualization, investigation, methodology, visualization, and writing–review and editing. M.O. was responsible for data acquisition, analysis, and writing–review and editing. C.S. contributed to writing–review and editing. J.M. participated in data acquisition and writing–review and editing. F.B. was involved in data acquisition and writing–review and editing. I.M. contributed to conceptualization, methodology, and supervision. B.V.L. contributed to conceptualization, writing–review and editing, supervision, and funding acquisition.

Data Availability Statement

The data that support the findings of this study are available from the corresponding author upon reasonable request.

Keywords

ionic conductivity, microstructure, pressure, slurry processing, solid electrolyte

Received: September 15, 2025
Revised: October 29, 2025
Published online: November 14, 2025

[1] J. B. Goodenough, K.-S. Park, *J. Am. Chem. Soc.* **2013**, *135*, 1167.
[2] Z. Yu, P. E. Rudnicki, Z. Zhang, Z. Huang, H. Celik, S. T. Oyakhire, Y. Chen, X. Kong, S. C. Kim, X. Xiao, H. Wang, Y. Zheng, G. A. Kamat, M. S. Kim, S. F. Bent, J. Qin, Y. Cui, Z. Bao, *Nat. Energy* **2022**, *7*, 94.
[3] X. He, D. Bresser, S. Passerini, F. Baakes, U. Krewer, J. Lopez, C. T. Mallia, Y. Shao-Horn, I. Cekic-Laskovic, S. Wiemers-Meyer, F. A. Soto, V. Ponce, J. M. Seminario, P. B. Balbuena, H. Jia, W. Xu, Y. Xu, C. Wang, B. Horstmann, R. Amine, C.-C. Su, J. Shi, K. Amine, M. Winter, A. Latz, R. Kostecki, *Nat. Rev. Mater.* **2021**, *6*, 1036.
[4] S. Liu, L. Zhou, J. Han, K. Wen, S. Guan, C. Xue, Z. Zhang, B. Xu, Y. Lin, Y. Shen, et al., *Adv. Energy Mater.* **2022**, *12*, 2200660.
[5] J. Janek, W. G. Zeier, *Nat. Energy* **2023**, *8*, 230.
[6] J. Janek, W. G. Zeier, *Nat. Energy* **2016**, *1*, 1.
[7] S. Li, J. Huang, Y. Cui, S. Liu, Z. Chen, W. Huang, C. Li, R. Liu, R. Fu, D. Wu, *Nat. Nanotechnol.* **2022**, *17*, 613.
[8] Z. Lu, Y. Guo, S. Zhang, S. Wu, R. Meng, S. Hong, J. Li, H. Xue, B. Zhang, D. Fan, Y. Zhang, C. Zhang, W. Lv, Q.-H. Yang, *Adv. Mater.* **2021**, *33*, 2101745.
[9] L. Ye, X. Li, *Nature* **2021**, *593*, 218.
[10] R. Koerver, I. Aygün, T. Leichtweiß, C. Dietrich, W. Zhang, J. O. Binder, P. Hartmann, W. G. Zeier, J. Janek, *Chem. Mater.* **2017**, *29*, 5574.
[11] P. Minnmann, F. Strauss, A. Bielefeld, R. Ruess, P. Adelhelm, S. Burkhardt, S. L. Dreyer, E. Trevisanello, H. Ehrenberg, T. Brezesinski, F. H. Richter, J. Janek, *Adv. Energy Mater.* **2022**, *12*, 2201425.
[12] Y.-G. Lee, S. Fujiki, C. Jung, N. Suzuki, N. Yashiro, R. Omoda, D.-S. Ko, T. Shiratsuchi, T. Sugimoto, S. Ryu, J. H. Ku, T. Watanabe, Y. Park, Y. Aihara, D. Im, I. T. Han, *Nat. Energy* **2020**, *5*, 299.
[13] R. Xu, J. Yue, S. Liu, J. Tu, F. Han, P. Liu, C. Wang, *ACS Energy Lett.* **2019**, *4*, 1073.
[14] J.-K. Hu, H. Yuan, S.-J. Yang, Y. Lu, S. Sun, J. Liu, Y.-L. Liao, S. Li, C.-Z. Zhao, J.-Q. Huang, *J. Energy Chem.* **2022**, *71*, 612.
[15] X. Hu, Z. Zhang, X. Zhang, Y. Wang, X. Yang, X. Wang, M. Fayena-Greenstein, H. A. Yehezkel, S. Langford, D. Zhou, B. Li, G. Wang, D. Aurbach, *Nat. Rev. Mater.* **2024**, *9*, 305.
[16] Y. Sakka, H. Yamashige, A. Watanabe, A. Takeuchi, M. Uesugi, K. Uesugi, Y. Orikasa, *J. Mater. Chem. A* **2022**, *10*, 16602.
[17] Y. Wu, S.-H. Bo, *ACS Appl. Energy Mater.* **2022**, *5*, 13571.
[18] V. Faka, M. T. Agne, M. A. Lange, D. Daisenberger, B. Wankmiller, S. Schwarzmüller, H. Huppertz, O. Maus, B. Helm, T. Böger, J. Hartel, J. M. Gerdes, J. J. Molaison, G. Kieslich, M. R. Hansen, W. G. Zeier, *J. Am. Chem. Soc.* **2024**, *146*, 1710.
[19] J.-M. Doux, H. Nguyen, D. H. Tan, A. Banerjee, X. Wang, E. A. Wu, C. Jo, H. Yang, Y. S. Meng, *Adv. Energy Mater.* **2020**, *10*, 1903253.
[20] A. Sakuda, A. Hayashi, M. Tatsumisago, *Sci. Rep.* **2013**, *3*, 2261.
[21] J. Lau, R. H. DeBlock, D. M. Butts, D. S. Ashby, C. S. Choi, B. S. Dunn, *Adv. Energy Mater.* **2018**, *8*, 1800933.
[22] M. Dixit, N. Muralidharan, A. Parejiya, C. Jafta, Z. Du, S. M. Neumayer, R. Essehli, R. Amin, M. Balasubramanian, I. Belharouak, *ACS Appl. Mater. Interfaces* **2022**, *14*, 44292.
[23] S. Randau, D. A. Weber, O. Kötz, R. Koerver, P. Braun, A. Weber, E. Ivers-Tiffée, T. Adermann, J. Kulisch, W. G. Zeier, F. H. Richter, J. Janek, *Nat. Energy* **2020**, *5*, 259.
[24] S. Ohno, T. Bernges, J. Buchheim, M. Duchardt, A.-K. Hatz, M. A. Kraft, H. Kwak, A. L. Santhosha, Z. Liu, N. Minafra, F. Tsuji, A. Sakuda, R. Schlem, S. Xiong, Z. Zhang, P. Adelhelm, H. Chen, A. Hayashi, Y. S. Jung, B. V. Lotsch, B. Roling, N. M. Vargas-Barbosa, W. G. Zeier, *ACS Energy Lett.* **2020**, *5*, 910.
[25] M. Cronau, M. Szabo, C. Konig, T. B. Wassermann, B. Roling, *ACS Energy Lett.* **2021**, *6*, 3072.
[26] X. Liu, B. Zheng, J. Zhao, W. Zhao, Z. Liang, Y. Su, C. Xie, K. Zhou, Y. Xiang, J. Zhu, H. Wang, G. Zhong, Z. Gong, J. Huang, Y. Yang, *Adv. Energy Mater.* **2021**, *11*, 2003583.
[27] X. Gao, B. Liu, B. Hu, Z. Ning, D. S. Jolly, S. Zhang, J. Perera, J. Bu, J. Liu, C. Doerrer, E. D. Darnbrough, D. Armstrong, P. S. Grant, P. G. Bruce, *Joule* **2022**, *6*, 636.
[28] W. J. Li, M. Hirayama, K. Suzuki, R. Kanno, *Mater. Trans.* **2016**, *57*, 549.
[29] Y. B. Song, H. Kwak, W. Cho, K. S. Kim, Y. S. Jung, K.-H. Park, *Curr. Opin. Solid State Mater. Sci.* **2022**, *26*, 100977.
[30] M. Yamamoto, Y. Terauchi, A. Sakuda, A. Kato, M. Takahashi, *J. Power Sources* **2020**, *473*, 228595.
[31] H. Kang, C. Lim, T. Li, Y. Fu, B. Yan, N. Houston, V. De Andrade, F. De Carlo, L. Zhu, *Electrochim. Acta* **2017**, *232*, 431.
[32] W. Zhang, D. Schröder, T. Arlt, I. Manke, R. Koerver, R. Pinedo, D. A. Weber, J. Sann, W. G. Zeier, J. Janek, *J. Mater. Chem. A* **2017**, *5*, 9929.
[33] R. Koerver, W. Zhang, L. De Biasi, S. Schweidler, A. O. Kondrakov, S. Kolling, T. Brezesinski, P. Hartmann, W. G. Zeier, J. Janek, *Energy Environ. Sci.* **2018**, *11*, 2142.

[34] T. Famprikis, P. Canepa, J. A. Dawson, M. S. Islam, C. Masquelier, *Nat. Mater.* **2019**, *18*, 1278.
[35] F. Hao, F. Han, Y. Liang, C. Wang, Y. Yao, *MRS Bull.* **2018**, *43*, 775.
[36] C. Lee, S. Y. Han, J. A. Lewis, P. P. Shetty, D. Yeh, Y. Liu, E. Klein, H.-W. Lee, M. T. McDowell, *ACS Energy Lett.* **2021**, *6*, 3261.
[37] M. S. Diallo, T. Shi, Y. Zhang, X. Peng, I. Shozib, Y. Wang, L. J. Miara, M. C. Scott, Q. H. Tu, G. Ceder, *Nat. Commun.* **2024**, *15*, 858.
[38] C. Hänsel, D. Kundu, *Adv. Mater. Interfaces* **2021**, *8*, 2100206.
[39] C. Hansel, P. V. Kumar, D. Kundu, *Chem. Mater.* **2020**, *32*, 10501.
[40] C. Xu, Z. Ahmad, A. Aryanfar, V. Viswanathan, J. R. Greer, *Proc. Natl. Acad. Sci. USA* **2017**, *114*, 57.
[41] M. J. Wang, R. Choudhury, J. Sakamoto, *Joule* **2019**, *3*, 2165.
[42] C. Schneider, C. P. Schmidt, A. Neumann, M. Clausnitzer, M. Sadowski, S. Harm, C. Meier, T. Danner, K. Albe, A. Latz, W. A. Wall, B. V. Lotsch, *Adv. Energy Mater.* **2023**, *13*, 2203873.
[43] R. Heckel, *Trans. Metal. Soc. AIME* **1961**, *221*, 671.
[44] J. Hersey, J. Rees, *Nat. Phys. Sci.* **1971**, *230*, 96.
[45] J. Ilkka, P. Paronen, *Int. J. Pharm.* **1993**, *94*, 181.
[46] M. Duberg, C. Nyström, *Powder Technol.* **1986**, *46*, 67.
[47] C. Sun, D. J. Grant, *Pharm. Dev. Technol.* **2001**, *6*, 193.
[48] R. Rowe, R. Roberts, in *Advances in Pharmaceutical Sciences*, vol. 7, 1–IV, Elsevier, **1995**.
[49] F. Mahmoodi, Ph.D. thesis, Acta Universitatis Upsaliensis, **2012**.
[50] S. Patel, A. M. Kaushal, A. K. Bansal, *Pharm. Res.* **2007**, *24*, 111.
[51] A.-K. Hatz, R. Calaminus, J. Feijoo, F. Treber, J. Blahusch, T. Lenz, M. Reichel, K. Karaghiosoff, N. M. Vargas-Barbosa, B. V. Lotsch, *ACS Appl. Energy Mater.* **2021**, *4*, 9932.
[52] C. Sedlmeier, T. Kutsch, R. Schuster, L. Hartmann, R. Bublitz, M. Tominac, M. Bohn, H. A. Gasteiger, *J. Electrochem. Soc.* **2022**, *169*, 070508.
[53] A. Tron, R. Hamid, N. Zhang, A. Paolella, P. Wulfert-Holzmann, V. Kolotygin, P. López-Aranguren, A. Beutl, *J. Energy Storage* **2023**, *66*, 107480.
[54] D. H. Nguyen, L. Grunenberg, I. Moudrakovski, K. Küster, B. V. Lotsch, *EES Batteries* **2025**, *1*, 824.
[55] C. A. Heck, T. Scharmann, M. Osenberg, A. Diener, I. Manke, P. Michalowski, A. Kwade, *Batteries & Supercaps* **2024**, *7*, e202300487.
[56] V. Faka, M. T. Agne, P. Till, T. Bernges, M. Sadowski, A. Gautam, K. Albe, W. G. Zeier, *Energy Advances* **2023**, *2*, 1915.
[57] T. Famprikis, Ö. U. Kudu, J. A. Dawson, P. Canepa, F. Fauth, E. Suard, M. Zbiri, D. Dambournet, O. J. Borkiewicz, H. Bouyanfif, S. P. Emge, S. Cretu, J.-N. Chotard, C. P. Grey, W. G. Zeier, M. S. Islam, C. Masquelier, *J. Am. Chem. Soc.* **2020**, *142*, 18422.
[58] W. Flygare, R. Huggins, *J. Phys. Chem. Solids* **1973**, *34*, 1199.
[59] R. Radzilowski, J. Kummer, *J. Electrochem. Soc.* **1971**, *118*, 714.
[60] P. C. Allen, D. Lazarus, *Phys. Rev. B* **1978**, *17*, 1913.
[61] K. S. Kim, W.-K. Paik, *J. Chem. Eng. Data* **1975**, *20*, 356.
[62] M. A. Plass, S. Bette, N. Philipp, I. Moundrakovski, K. Küster, R. E. Dinnebier, B. V. Lotsch, *J. Mater. Chem. A* **2023**, *11*, 13027.
[63] M. A. Plass, S. Bette, R. E. Dinnebier, B. V. Lotsch, *Chem. Mater.* **2022**, *34*, 3227.
[64] S. Ohno, B. Helm, T. Fuchs, G. Dewald, M. A. Kraft, S. P. Culver, A. Senyshyn, W. G. Zeier, *Chem. Mater.* **2019**, *31*, 4936.
[65] M. A. Kraft, S. P. Culver, M. Calderon, F. Böcher, T. Krauskopf, A. Senyshyn, C. Dietrich, A. Zevalkink, J. Janek, W. G. Zeier, *J. Am. Chem. Soc.* **2017**, *139*, 10909.
[66] T. Bernges, S. P. Culver, N. Minafra, R. Koerver, W. G. Zeier, *Inorg. Chem.* **2018**, *57*, 13920.
[67] W. v. Meyer, H. Neldel, *Z. tech. Phys* **1937**, *18*, 588.
[68] S. Muy, J. C. Bachman, H.-H. Chang, L. Giordano, F. Maglia, S. Lupart, P. Lamp, W. G. Zeier, Y. Shao-Horn, *Chem. Mater.* **2018**, *30*, 5573.